

Multi-frequency Data Parallel Spin Wave Logic Gates

Abdulqader Mahmoud,^{1, a)} Frederic Vanderveken,^{2, 3} Christoph Adelman,³ Florin Ciubotaru,³ Said Hamdioui,¹ and Sorin Cotofana^{1, b)}

¹⁾*Delft University of Technology, Department of Quantum and Computer Engineering, 2628 CD Delft, The Netherlands*

²⁾*KU Leuven, Department of Materials, SIEM, 3001 Leuven, Belgium*

³⁾*Imec, 3001 Leuven, Belgium*

By their very nature, Spin Waves (SWs) with different frequencies can propagate through the same waveguide without affecting each other, while only interfering with their own species. Therefore, more SW encoded data sets can coexist, propagate, and interact in parallel, which opens the road towards hardware replication free parallel data processing. In this paper, we take advantage of these features and propose a novel data parallel spin wave based computing approach. To explain and validate the proposed concept, byte-wide 2-input XOR and 3-input Majority gates are implemented and validated by means of Object Oriented MicroMagnetic Framework (OOMMF) simulations. Furthermore, we introduce an optimization algorithm meant to minimize the area overhead associated with multifrequency operation and demonstrate that it diminishes the byte-wide gate area by 30% and 41% for XOR and Majority implementations, respectively. To get inside on the practical implications of our proposal we compare the byte-wide gates with conventional functionally equivalent scalar SW gate based implementations in terms of area, delay, and power consumption. Our results indicate that the area optimized 8-bit 2-input XOR and 3-input Majority gates require 4.47x and 4.16x less area, respectively, at the expense of 5% and 7% delay increase, respectively, without inducing any power consumption overhead. Finally, we discuss factors that are limiting the currently achievable parallelism to 8 for phase based gate output detection and demonstrate by means of OOMMF simulations that this can be increased 16 for threshold based detection based gates.

^{a)}Electronic mail: a.n.n.mahmoud@tudelft.nl

^{b)}Electronic mail: S.D.Cotofana@tudelft.nl

I. INTRODUCTION

The amount of row data has rapidly increased in the last few decades due to the information technology unprecedented growth. These data are usually processed on high efficiency CMOS technology based computing platforms¹⁻³ and as the amount of row data increased, technology feature size has been shrunken to keep up with the computation power demands. However, when entering into the deca-nanometer regime CMOS downscaling becomes more difficult due to: (i) leakage wall^{4,5}, (ii) reliability wall⁶, and (iii) cost wall^{4,6}, which suggests the near end of Moore's law. As a result, different technologies, e.g., graphene⁷⁻¹¹, memristor¹²⁻¹⁶, spintronics¹⁷⁻²¹ have been explored in an attempt to meet the exponentially increasing computing market demands²².

While each of these alternative technologies exhibits both strong and weak points, spintronics on its Spin Wave (SW) flavour seems to have a great potential to meet market needs²² due to its: (i) Ultra-low power consumption as no charge movements are required in order to perform calculations, (ii) acceptable delay, (iii) down to nm range scalability, and (iv) natural support for data parallelism enabled by the fact that SWs of different frequency can coexist and selectively interact within the same waveguide.

In view of this, different logic gates built on spin wave technology were presented, e.g.,²³⁻⁴², and in the sequel we briefly present some of them. A current controlled Mach-Zender interferometer based NOT gate has been the first experimentally demonstrated SW logic gate²³ and by making use of a similar method, other logic gates including XNOR, NAND, and NOR were realized²⁴⁻²⁶. NOT, OR, and AND gates were designed using three terminal devices with transmission lines^{27,28,29,30} and voltage-controlled XNOR and NAND gates utilizing re-configurable nano-channel magnonic devices were suggested³¹. In addition, an XOR gate was proposed by embedding magnon transistors between the Mach-Zehnder interferometer arms³². By relying on another information encoding method, i.e., on SW phase rather than on SW amplitude as it is the case for the previously mentioned schemes, buffer, NOT, (N)AND, (N)OR, XOR, and Majority gates were introduced in³³. Moreover, alternative Majority gate designs were suggested to decrease the SW back propagation and increase the SW transmission efficiency³⁴⁻³⁶. OR and NOR gates were designed using cross structures³⁷ and physically implemented Majority gates were reported in³⁸⁻⁴¹.

All the previously mentioned designs operate on same frequency SWs, i.e., on 1-bit inputs,

therefore, if multiple-bit input functions are to be evaluated, e.g., bitwise XOR over two n -bit inputs $A = (a_1, a_2, \dots, a_n)$ and $B = (b_1, b_2, \dots, b_n)$, an XOR gate structure must be replicated n times in order to process the n input bit-pairs (sets) in parallel at the expense of area overhead. However, different frequency SWs can simultaneously propagate through the same waveguide without affecting each other, while only interfering with their own species. This suggests that if each input pair (a_i, b_i) is encoded with f_i frequency SWs, $\text{XOR}(A, B)$ can be potentially evaluated with one instead of n XOR gates. This approach has been pursued in⁴², which introduces a Majority gate structure able to simultaneously process 3 data set encoded at 3 different frequencies. However, the suggested structure make use of bent regions, which have detrimental effects on SW propagation, and contains a magnonic crystal that induces a large delay overhead.

In this paper we revisit the SW parallelism concept and propose a novel multi-frequency data parallel in-line generic SW gate structure. Our contributions can be summarized as follows:

- Generic multi-frequency data parallel in-line SW gate structure and an associated area optimization algorithm.
- Design and validation of 8-bit data parallel in-line Spin Wave logic gates: 8-bit 3-input Majority and 2-input XOR gates are instantiated and validated by means of Object Oriented MicroMagnetic Framework (OOMMF) simulations.
- Performance assessment and comparison with SW state-of-the-art: The proposed 8-bit 3-input Majority and 2-input XOR gates require 4.47x and 4.16x less area, respectively, when compared with functionally equivalent scalar SW gate based implementations, at the expense of 5% and 7% delay penalty, respectively, and no power consumption overhead.
- Parallelism limit study: Demonstrate by means of OOMMF simulation that the maximum currently achievable parallelism, i.e., the number of different SW frequencies, is 8 for phase based output detection and 16 when spin wave magnetization is utilized to detect the gate output.

- Design and OOMMF validation of a 16-bit data parallel in-line Spin Wave 2-input XOR gate.

The remainder of the paper is organized as follows. Section II briefly explains the SW physics fundamentals and the associated computing paradigm. Section III describes the proposed n -bit data parallel SW logic gate and introduces the associated area optimization algorithm. Section IV provides inside on the utilized simulation platform and parameters, and presents simulation experiments related to the validation of the 8-bit 3-input Majority and 2-input XOR gates. Section V presents evaluation results for the two byte wide parallel gates and a comparison with functional equivalent scalar implementations. In addition, it discusses fan-in and geometric scalability, and maximum achievable parallelism issues, and variability and thermal noise effects. Section VI concludes the paper.

II. SW BASED COMPUTING BACKGROUND

When a ferromagnetic material is exposed to an external magnetic field electron spins arrange themselves in the applied magnetic field direction, in order to bring the total system energy to the lowest possible level⁴³. Further, if the electron spins are deflected by an excitation method, e.g., by means of Magnetolectric (ME) cell, antenna, a Spin Wave (SW) is created mainly due to exchange and dipole spin interactions. The precessional electron spin movement⁴³, can be described by the Landau-Lifshitz-Gilbert (LLG) relation^{44,45} as follows:

$$\frac{d\vec{m}}{dt} = -|\gamma|\mu_0 \left(\vec{m} \times \vec{H}_{eff} \right) + \alpha \left(\vec{m} \times \frac{d\vec{m}}{dt} \right), \quad (1)$$

where γ is the gyromagnetic ratio, μ_0 the vacuum permeability, α the damping factor, m the magnetization, and H_{eff} the effective field and it is expressed as:

$$H_{eff} = H_{ext} + H_{ex} + H_{demag} + H_{ani}, \quad (2)$$

where H_{ext} is the external field, H_{ex} the exchange field, H_{demag} the demagnetizing field, and H_{ani} the magneto-crystalline anisotropy.

An excited SW is characterised by its wavelength λ (the shortest distance between similar consecutive spins), wave number k ($k = \frac{2*\pi}{\lambda}$), frequency f (determined by the complete spin precession time), phase ϕ , and amplitude A , as graphically indicated in Figure 1. As such, an SW can carry information encoded in its amplitude, phase, frequency, or a combination of

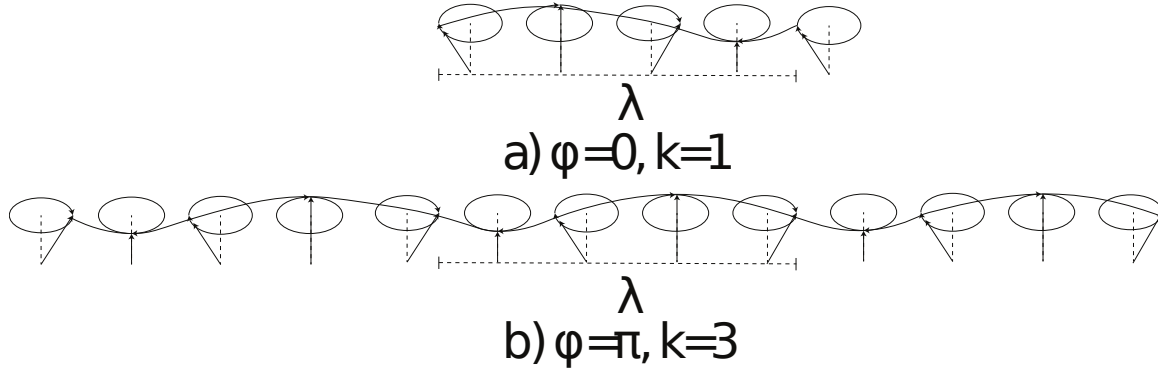


FIG. 1. SW Parameters

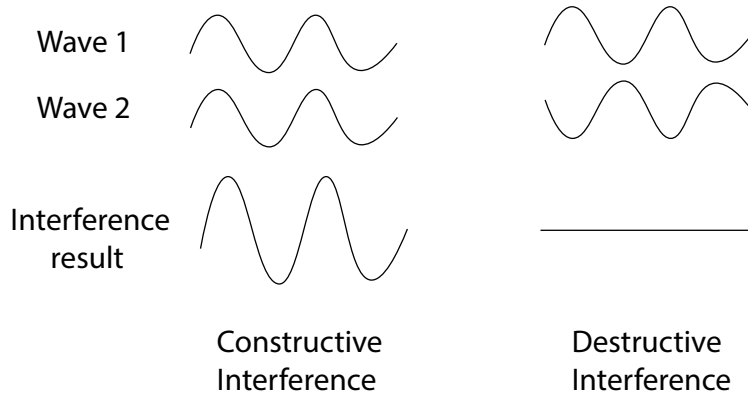


FIG. 2. Wave Interference.

them. Once formed, the SW propagates through the ferromagnetic material (waveguide) and may eventually meet other SWs present in the waveguide, case in which their interaction is governed by the wave interference principles. For instance, if two SWs with the same amplitude, wavelength, and frequency coexist in a waveguide, they interfere constructively if they have the same phase, and destructively if they are out of phase ($\Delta\phi = \pi$) as depicted in Figure 2. Furthermore, if more than two waves having the same A , f , and λ interfere in the waveguide, the outcome captures a majority decision, i.e., if the number of spin waves having $\phi = 0$ is larger than the number of spin waves having $\phi = \pi$, the resulting spin wave has $\phi = 0$, and $\phi = \pi$ otherwise. Thus, SW interference provides natural support for direct Majority gate implementations, e.g., 3-input Majority is evaluated by means of a 3-SW interference in a waveguide³³, while its CMOS based implementation requires 18 transistors. Moreover, SWs with different frequencies can coexist and propagate in the same waveguide without affecting each other and only interacting with other same-frequency SWs,

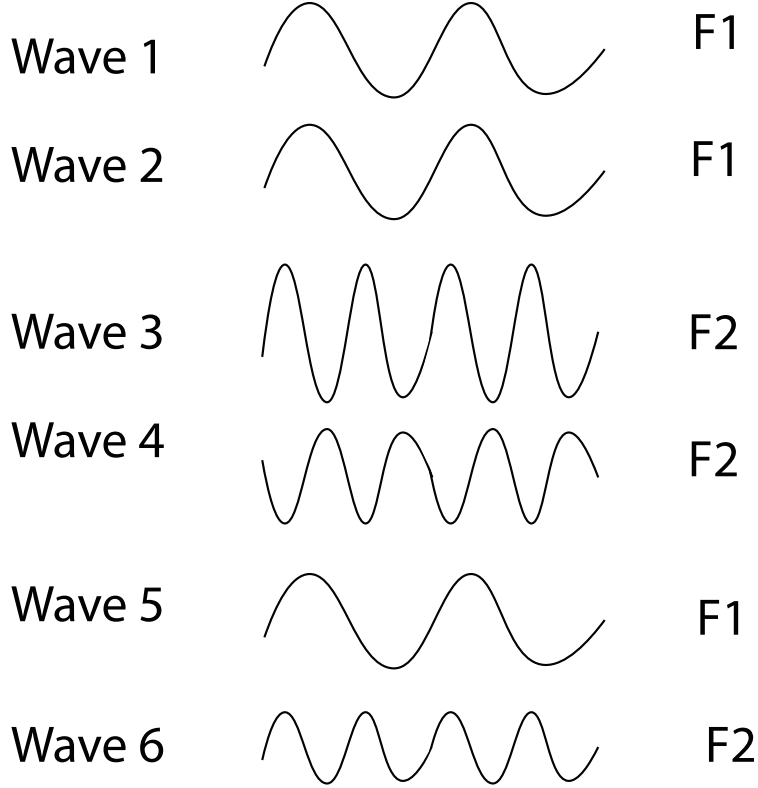


FIG. 3. Different Frequency, Wavelength, and Amplitude Spin Wave Interference.

which indicates that SW interaction provides intrinsic support for data parallel computing. Note that, in the most general case, spin waves with different amplitude, frequency, and wavelength can coexist and selectively interfere in the same waveguide, which results in more complex interference patterns as presented in Figure 3. As depicted in the Figure, f_1 waves F1 and F2 interference results in F5 and f_2 waves F3 and F4 interference results in F6, while no interaction between the f_1 and f_2 waves occurs. We note that in our investigation we consider that regardless of their frequency all input SWs have the same amplitude.

Depending on the orientation relation between spin wave propagation, effective magnetic field, and magnetization three main Magnetostatic Spin Wave (MSW) types exist: Magnetostatic Surface Spin Wave (MSSW), Forward Volume Magnetostatic Spin Wave (FVMSW), and Backward Volume Magnetostatic Spin Wave (BVMSW)⁴³. While each type has certain interesting properties, FVMSWs are the most attractive as in-plane spin-wave propagation is isotropic, which is beneficial from the circuit design prospective.

Figure 4 depicts the generic structure of a SW based logic gate, which consists of multiple

inputs ($I_1, I_2, I_3, \dots, I_n$), a Functional Region (FR), which might perform Majority, AND, OR, XOR function or its inverted version, and an output O . All inputs are excited at the same frequency, propagate from their sources through the waveguide and interfere constructively or destructively based on their phases. The result is available at the output as a SW with the same frequency as the inputs. This is a scalar gate as each input SW represents one bit, thus in case the same function has to be pairwise evaluated on n -bit inputs this can be done in parallel by instantiating n such gates or serially by using one gate only with the associated area and delay overhead, respectively. In the following section we take advantage of different frequency SW interaction behaviour and introduce data parallel SW gates that can process n -bit inputs without hardware replication or serialisation.

III. n -BIT DATA PARALLEL SW LOGIC GATE

Figure 5 presents the parallel spin wave logic gate we introduced in⁴⁶, which is able to concurrently process m n -bit inputs. As indicated in the Figure, the input sets $\mathcal{I}_i = \{I_{i,1}, I_{i,2}, I_{i,3}, \dots, I_{i,m}\}, i = 1, 2, \dots, n$, are simultaneously encoded into SWs with frequency f_i by means of, e.g., Magnetolectric (ME) cells or antennas. Subsequently, the SWs corresponding the sets $\mathcal{I}_i, i = 1, 2, \dots, n$ propagate through the waveguide without affecting each other until reaching the Functional Region (FR). Once the $m \times n$ spin waves arrive at FR, equal-frequency spin waves interfere constructively and destructively depending on their phases, producing n output SWs $\mathcal{O}_i = \mathcal{F}(\mathcal{I}_i), i = 1, 2, \dots, n$, where \mathcal{F} is the gate function, e.g., AND, OR, XOR. Those SWs can be sensed and transformed into the voltage domain by the detection cells located at O_1, O_2, \dots, O_n or transmitted to the next SW gate.

Although the approach in Figure 5 is generic its practical realization requires stacked waveguides and contains bent regions, which impede smooth SW propagation. We address

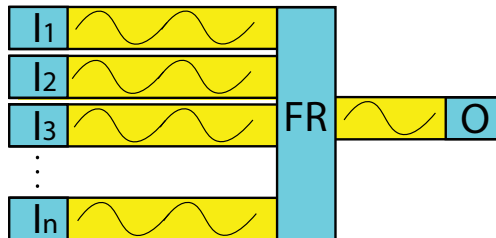


FIG. 4. Conventional SW Logic Gate Structure

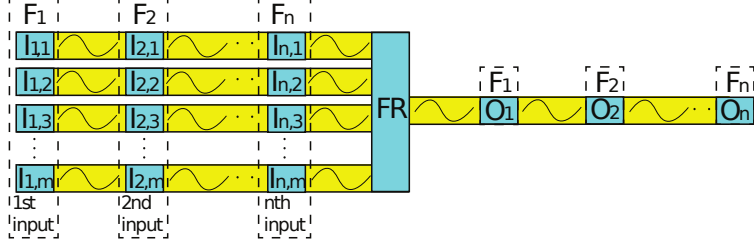


FIG. 5. Multi-Frequency Spin Wave Logic Gate

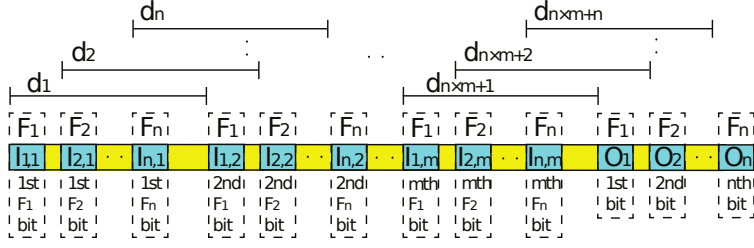


FIG. 6. n -bit Inputs In-line Spin Wave Logic Gate

these issues by apply the same idea on a single waveguide structure and constructing the in-line gate in Figure 6.

Note that for proper gate operation, SWs with the same frequency must be excited with the same amplitude and wavelength. Moreover, the distances between input sources and interference locations are SW frequency specific and crucial for proper gate functionality, thus they must be accurately determined. For example, if constructive interference is required for in-phase SWs and destructive for out of phase SWs, the distances between the same frequency sources must be $j_q \times \lambda_i, i = (1, 2, 3, \dots, n)$, i.e., $d_1 = j_1 \lambda_1, d_2 = j_2 \lambda_2, \dots, d_{nm} = j_{nm} \lambda_n$, where $j_q = \{1, 2, 3, \dots\}, q = 1, 2, 3, \dots, nm$. Note that to minimize gate area and delay $j_q = 1$ is the preferred choice, which is feasible for scalar gates but not always possible for parallel gates. Whereas, the distances must be $(j_q + \frac{1}{2})\lambda_i$, i.e., $d_1 = (j_1 + \frac{1}{2})\lambda_1, d_2 = (j_2 + \frac{1}{2})\lambda_2, \dots, d_{nm} = (j_{nm} + \frac{1}{2})\lambda_n$, if the opposite behaviour is desired.

In view of the previous discussion each output wave O_i is available for detection after a delay determined by the distance between the most faraway input cell of the \mathcal{I}_i set, i.e., $I_{i,1}$ in Figure 6, and the output cell O_i , thus full parallelism is achieved. Note that the actual gate delay value can be optimized by choosing appropriate, e.g., waveguide material, dimensions, thickness, as discussed in Section IV.

While delay optimization is a matter of waveguide material and geometry choice, the

gate area can be minimized by changing the position of the input and output transducers. One can observe in Figure 6 that input and output cells are ordered by bit position for clarity purpose. However, they can be shuffled as long as the previously discussed constraints are still satisfied, and this results in an area (overall gate length) reduction. To this end we introduce Algorithm 1, which identifies the transducer (source/detector) locations that are minimizing the waveguide length, while not infringing the wavelength dependent inter transducers distance constraints. The algorithm iteratively construct the gate structure by instantiating one input set $\mathcal{I}_i, i = 1, 2, \dots, n$ at a time, while optimizing its transducer positions in relation to the already optimized structure embedding the previously instantiated sets $\mathcal{I}_j, j = 1, 2, \dots, i - 1$.

The algorithm starts with a configuration in which all transducers are placed overlapped at the waveguide beginning. Subsequently, inputs sets are processed one at a time by initially placing them one after the other at D distance regardless of the wavelength of the SW they process (line 3 to 7). If the first set was the one currently processed no further adjustments are required and the second set can be considered for placement. If this is not the case, the for loop (line 9 to 24) is repositioning the transducer at the correct positions, which are multiples of their wavelength frequency. After this step, the transducer configuration for the up to date processed sets is the same as in Figure 6. Next, the for loop (line 25 to 38) performs the area optimization by checking the spaces between transducers and if it is possible moving one transducer if its wavelength imposed distance condition is satisfied. If one transducer has been moved **Sort** reorders the transducers in the **TP** matrix to capture the new configuration. These steps are repeated until all sets are placed and the gate length optimized. At the end, the gate area is calculated by multiplying the waveguide width by the waveguide length.

Let us assume a 3-bit 2-input gate operating on SWs with wavelength $\lambda_1=100$ nm, $\lambda_2=50$ nm, and $\lambda_3=19$ nm, 10 nm transducer length, and 1 nm minimum distance between transducers. By following the structure in Figure 6, the second input set can begin at 33 nm from the waveguide start because the first three sources $I_{1,1}, I_{1,2}, I_{1,3}$ occupy each 10 nm and are 1 nm distanced apart. As such the initial order is $(I_{1,1}, I_{1,2}, I_{1,3}, I_{2,1}, I_{2,2}, I_{2,3}, O_1, O_2, O_3)$ with a corresponding waveguide length of 288 nm. The optimization algorithm changes the order to $(I_{1,1}, I_{1,2}, I_{1,3}, I_{2,3}, I_{2,2}, I_{2,1}, O_3, O_2, O_1)$, which corresponds to a 210 nm waveguide length thus about 27% area savings.

Algorithm 1 Data Parallel Gate Area Optimization

Inputs: WE, L, D, w, $d[i]$, $i=1:n$, $\lambda[i]$, $i=1:n$ **Outputs:** $TP[i,j]$, $i=1:n$; $j=1:m+1$, A ▷ WE is the waveguide end, L the transducer length, D the minimum distance between consecutive transducers, w the waveguide width, d the distance between two consecutive inputs of the same frequency, TP is the transducer position, A is the gate area.

```

1:  $TP[1:n,1:m+1] = 0$ 
2:  $WE = 0$ 
3: for  $j = 1$  to  $m + 1$  do
4:   for  $i = 1$  to  $n$  do
5:      $TP[i,j] = WE$ 
6:      $WE = WE + L + D$ 
7:   end for
8:   if  $j > 1$  then
9:     for  $i = 1$  to  $n$  do
10:       $d[i] = TP[i,j] - TP[i,j-1]$ 
11:      if  $\left\lceil \frac{d[i]}{\lambda[i]} \right\rceil \times \lambda_i = d[i]$  then
12:         $TP[i,j] = TP[i,j]$ 
13:      else
14:         $TP[i,j] \leftarrow \left\lceil \frac{d[i]}{\lambda[i]} \right\rceil \times \lambda[i]$ 
15:      end if
16:      if  $i = 1$  then
17:         $TP[i-1,j] = TP[n,j-1]$ 
18:      end if
19:      if  $TP[i,j] - TP[i-1,j] > D + L$  then
20:         $TP[i,j] = TP[i,j]$ 
21:      else
22:         $TP[i,j] = TP[i,j] + \lambda[i]$ 
23:      end if
24:    end for
25:    for  $i = 1$  to  $n$  do
26:      if  $i = 1$  then
27:         $TP[i-1,j] = TP[n,j-1]$ 
28:      end if
29:      if  $TP[i,j] - TP[i-1,j] > D + L$  then
30:        for  $c = 1$  to  $n$  do
31:          if  $\left\lceil \frac{TP[i,j]+D+L}{\lambda[c]} \right\rceil \times \lambda[c] = TP[i,j]+D+L$  then
32:             $TP[c,j] = TP[i,j] + D + L$ 
33:             $TP \leftarrow \text{Sort}(TP)$ 
34:          end if
35:        end for
36:      end if
37:    end for
38:  end if
39: end for
40:  $WE = TP[n,m+1] + L$ 
41:  $A = WE \times w$ 

```

Furthermore, two main methods can be utilized for output detection: (i) Phase detection, and (ii) Threshold detection. In the first case, a predefined phase is utilized as reference and a phase difference of 0 represents a logic 0, and a phase difference of π a logic 1. The second detection method assesses the SW magnetization (SWM) value and reports a 0 logic if the SWM is smaller than a predefined threshold value and a logic 1 otherwise. If phase detection is in place, the gate can provide non-inverted or inverted output (or even both of them) by adjusting the reading location. For instance, referring to Figure 6, the detectors must be placed at a distance equal to (from the last f_i SW source) $(j_q + \frac{1}{2})\lambda_i, i = (1, 2, 3, \dots, n)$, such that $d_{nm+1} = (j_{nm+1} + \frac{1}{2})\lambda_1, d_{nm+2} = (j_{nm+2} + \frac{1}{2})\lambda_2, \dots, d_{nm+n} = (j_{nm+n} + \frac{1}{2})\lambda_n$, if the non-inverted results are desired. However, the detectors must be placed at a distance equal to (from the last f_i SW sources) $j\lambda_i$ such that $d_{nm+1} = j_{nm+1}\lambda_1, d_{nm+2} = j_{nm+2}\lambda_2, \dots, d_{nm+n} = j_{nm+n}\lambda_n$ if the compliment is required. In the case of threshold based detection, the gate can provide non-inverted or inverted outputs without changing the output detector position by just switching the thresholding condition in the detector cell. Note that, regardless of the detection method, each read location should be as close as possible to the last input in its set to diminish the due to damping SW energy lost and process high amplitude spin waves.

IV. SIMULATION SETUP

This section provides inside on the simulation platform, parameters, and performed experiments.

A. Simulation Platform

The Object Oriented MicroMagnetic Framework (OOMMF)⁴⁷ is utilized to evaluate the proposed structures. OOMMF numerically solves the LLG equation to capture the gate behaviour. The OOMMF input is a TCL/TKL script, which describes the gate and the input stimuli and the results can be visualized within the OOMMF framework or post-processed by other tools like matlab, which is the case in this paper.

TABLE I. Parameters

Parameters	Values
Magnetic saturation M_s	1.1×10^6 A/m
Perpendicular anisotropy constant k_{ani}	8.3177×10^5 J/m ³
Damping constant α	0.004
Waveguide thickness t	1 nm
Exchange stiffness A_{exch}	18.5 pJ/m

B. Simulation Parameters

$Fe_{60}Co_{20}B_{20}$ waveguides that have waveguide width of 50 nm with Perpendicular Magnetic Anisotropy (PMA) are utilized for all gate constructions. We note that for this material the anisotropy field $H_{anisotropy} > M_s$, which means that there is no need for the application of an external magnetic field⁴⁸. Table I presents the parameter we utilize to validate the 8-bit 2-input XOR/XNOR and 3-input Majority gates. The 8 SW frequencies are 10 GHz, 20 GHz, 30 GHz, 40 GHz, 50 GHz, 60 GHz, 70 GHz, and 80 GHz. By making use of the FVMSW dispersion relation and given that the wavenumber $k = \frac{2\pi}{\lambda}$, we determine the distances between transducers exciting/detecting SWs with the same frequency are: $d_1=166$ nm (j=2), $d_2=100$ nm (j=2), $d_3=117$ nm (j=3), $d_4=165$ nm (j=5), $d_5=174$ nm (j=6), $d_6=130$ nm (j=5), $d_7=168$ nm (j=7), and $d_8=176$ nm (j=8). Furthermore, an 1 nm minimum separation distance between transducers is in place.

C. Performed Simulations

We perform the following simulation experiments:

- 8-bit 2-input XOR/XNOR gate with threshold detection. The two 8-bit inputs are simultaneously excited using the sources $(I_{1,1}, I_{2,1}, I_{3,1}, \dots, I_{8,2})$. The excited spin waves propagate through the waveguide and those who have the same frequencies interfere with each other. The resulting spin waves propagate towards the output where they are captured at O_1, O_2, \dots, O_8 based on threshold detection. We carry on the validation of both area unoptimized $(I_{1,1}, I_{2,1}, I_{3,1}, I_{4,1}, I_{5,1}, I_{6,1}, I_{7,1}, I_{8,1}, I_{1,2}, I_{2,2}, I_{3,2}, I_{4,2}, I_{5,2}, I_{6,2}, I_{7,2}, I_{8,2}, I_{1,3}, I_{2,3}, I_{3,3}, I_{4,3}, I_{5,3}, I_{6,3}, I_{7,3}, I_{8,3})$ and optimized

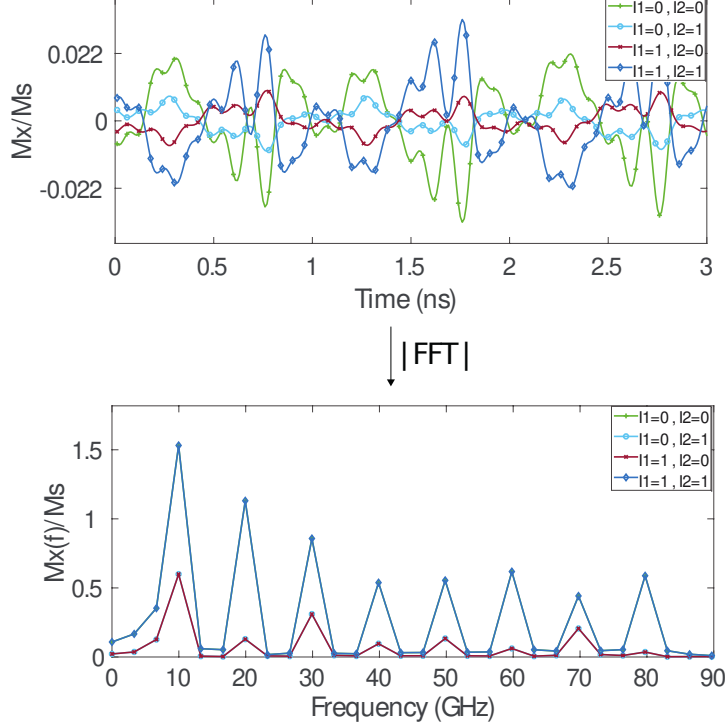


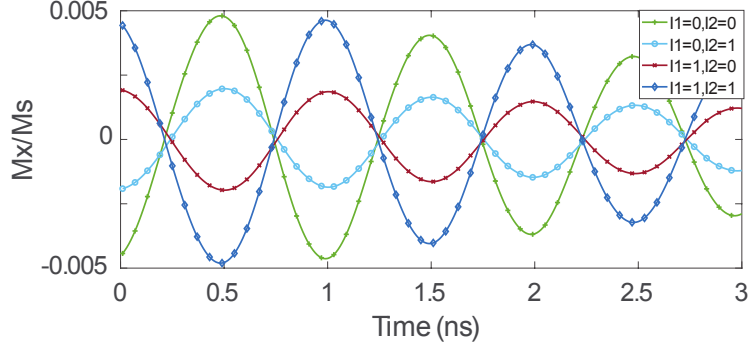
FIG. 7. Unoptimized 8-bit XOR Gate Time and Frequency Response.

($I_{1,1}, I_{2,1}, I_{3,1}, I_{4,1}, I_{5,1}, I_{6,1}, I_{7,1}, I_{8,1}, I_{2,2}, I_{3,2}, I_{1,2}, I_{6,2}, I_{4,2}, I_{5,2}, I_{7,2}, I_{8,2}, I_{2,3}, I_{8,3}, I_{3,3}, I_{1,3}, I_{6,3}, I_{4,3}, I_{5,3}, I_{7,3}$) configurations. Note that as detectors order is not important they follow the same pattern, i.e., ($O_1, O_2, O_3, O_4, O_5, O_6, O_7, O_8$) in both cases.

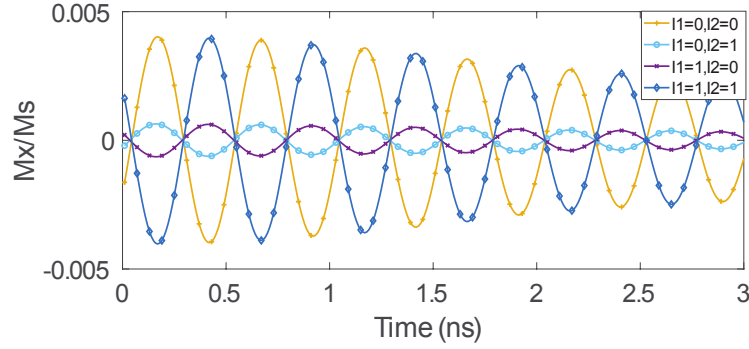
- 8-bit 3-input Majority gate based on phase detection. We again considered area unoptimized and optimized gate instances but in this case detector order is relevant, thus the after optimization source and detector order is $I_{1,1}, I_{2,1}, I_{3,1}, I_{4,1}, I_{5,1}, I_{6,1}, I_{7,1}, I_{8,1}, I_{2,2}, I_{3,2}, I_{1,2}, I_{6,2}, I_{4,2}, I_{5,2}, I_{7,2}, I_{8,2}, I_{2,3}, I_{8,3}, I_{3,3}, I_{1,3}, I_{6,3}, I_{4,3}, I_{5,3}, I_{7,3}, O_6, O_8, O_4, O_2, O_5, O_1, O_7, O_3$.

V. SIMULATION RESULTS AND DISCUSSION

This section presents simulation results for the 8-bit 2-input XOR/XNOR and 3-input Majority gate instances, performance estimations, and a comparison with SW state-of-the-art functionally equivalent structures. Subsequently, it discusses fan-in and geometric scalability, and maximum achievable parallelism (upper bound of the number of practically achievable SW frequencies) issues, and variability and thermal noise effects.

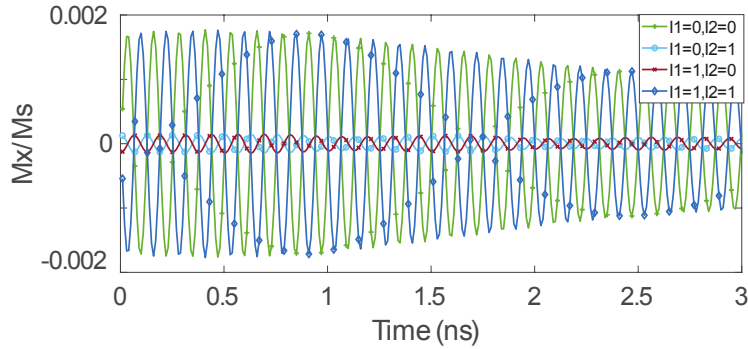


(a) $F_1=10\text{GHz}$



(b) $F_2=20\text{GHz}$

•
•



(h) $F_8=80\text{GHz}$

FIG. 8. Unoptimized 8-bit XOR Gate Outputs a) $f_1=10\text{ GHz}$, b) $f_2=20\text{ GHz}$, ..., h) $f_8=80\text{ GHz}$.

A. Simulation Results

8-bit 2-input threshold detection based XOR/XNOR gate

Figure 7 presents OOMMF simulation results for the area unotimized byte-based 2-input XOR gate instance. The y -axis reflects the output SWs M_x over M_s ratio, i.e., magnetization

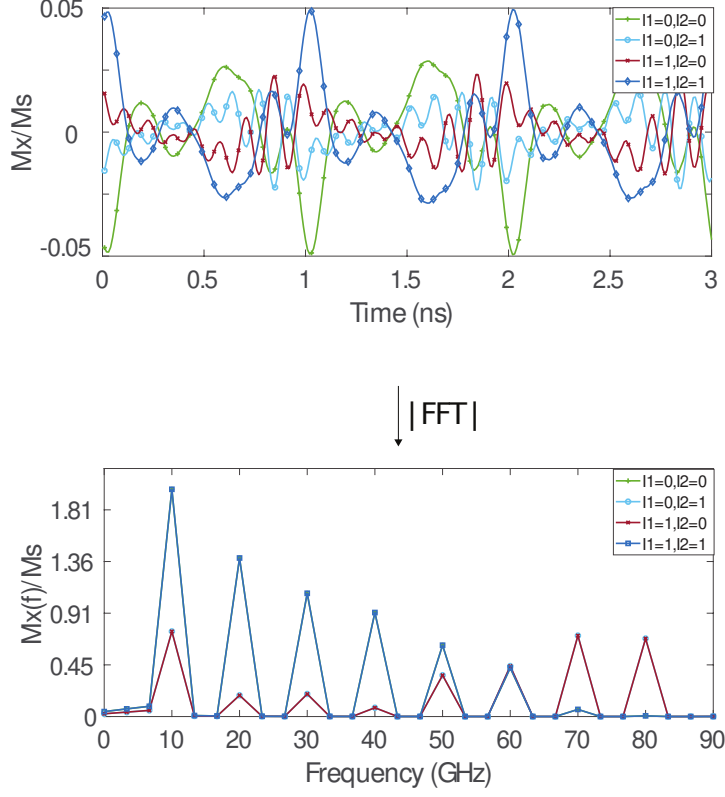
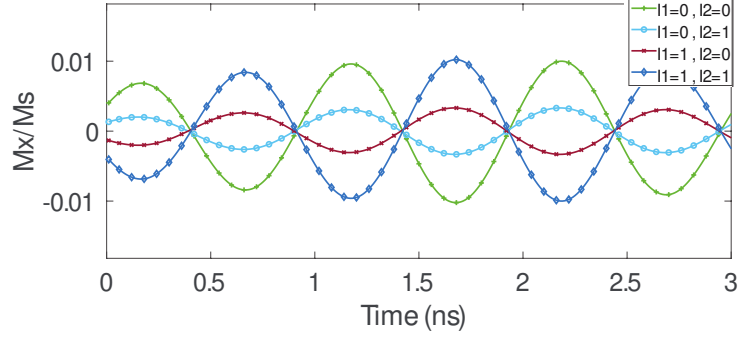
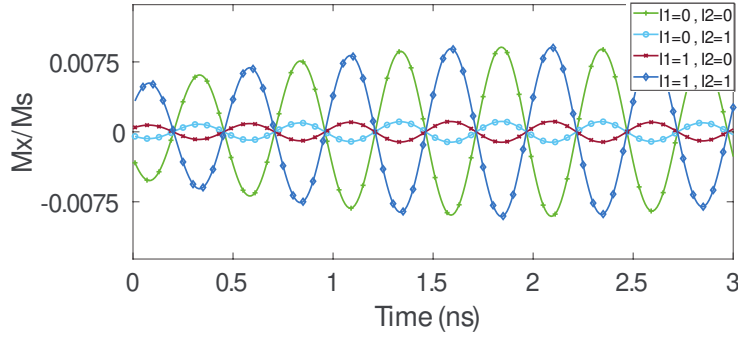


FIG. 9. Optimized 8-bit XOR Gate Time and Frequency Response.

in the x -direction over magnetic saturation. To simplify the Figure we only assume all 0s and all 1s input sets, thus only four input combinations are possible, and as such the gate response to any input combination is the same in all frequencies. As expected same-frequency SW pairs interfere without affecting the other SWs and this is clear from Figure 7, which indicates that 8 different frequencies components exist without distorting each-other in the Fast Fourier Transform (FFT) amplitude spectrum for all the considered input combinations. Moreover, as it can be noticed from Figure 8, the output SWs are not distorted and can be properly detected for each frequency. Let us consider the first output detection cell, which is tuned for the 10 GHz SW. When reading the output at time 0.5 ns for $\mathcal{I}_1 = \mathcal{I}_2 = 0$ and $\mathcal{I}_1 = \mathcal{I}_2 = 1$, the absolute SW magnetization value is greater than $0.0035 M_s$ due to the constructive interference, whereas the SW magnetization is less than $0.0035 M_s$ when one input set is 0 and the other one is 1. Therefore, if the detection threshold is set to $0.0035 M_s$ an XOR function is obtained as a SW magnetization greater (lower) than $0.0035 M_s$ is read as a logic 0 (1). An XNOR can be realized by flipping the condition such that a SW magnetization lower (greater) than $0.0035 M_s$ is read as a logic 0 (1). Similarly, for the

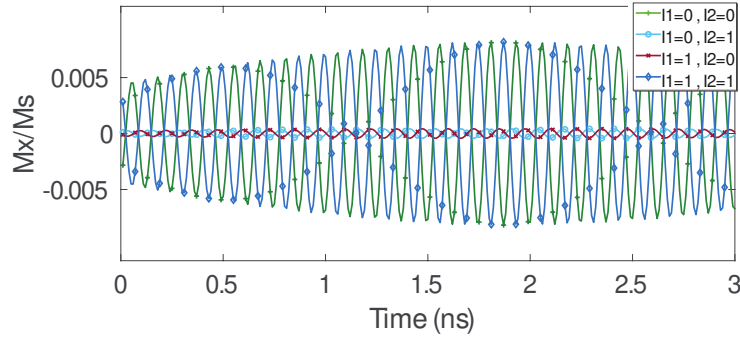


(a) $F_1=10\text{GHz}$



(b) $F_2=20\text{GHz}$

⋮



(h) $F_8=80\text{GHz}$

FIG. 10. Optimized 8-bit XOR Gate Outputs: a) $f_1=10\text{ GHz}$, b) $f_2=20\text{ GHz}$, \dots , h) $f_8=80\text{ GHz}$.

second detection cell, which targets the 20 GHz SW a threshold value of $0.0032 M_s$ is in place and by following a similar way of reasoning threshold values of $0.0028 M_s$, $0.0025 M_s$, $0.0022 M_s$, $0.0017 M_s$, $0.0015 M_s$, and $0.001 M_s$ can be determined for the rest of frequencies.

Figure 9 and 10 present OOMMF simulation results for the optimized 8-bit 2-input XOR gate. As depicted in Figure 10, the simulation proves the correct functionality of the XOR/XNOR gate. One can observe in the Figure that in this case the SW magnetization

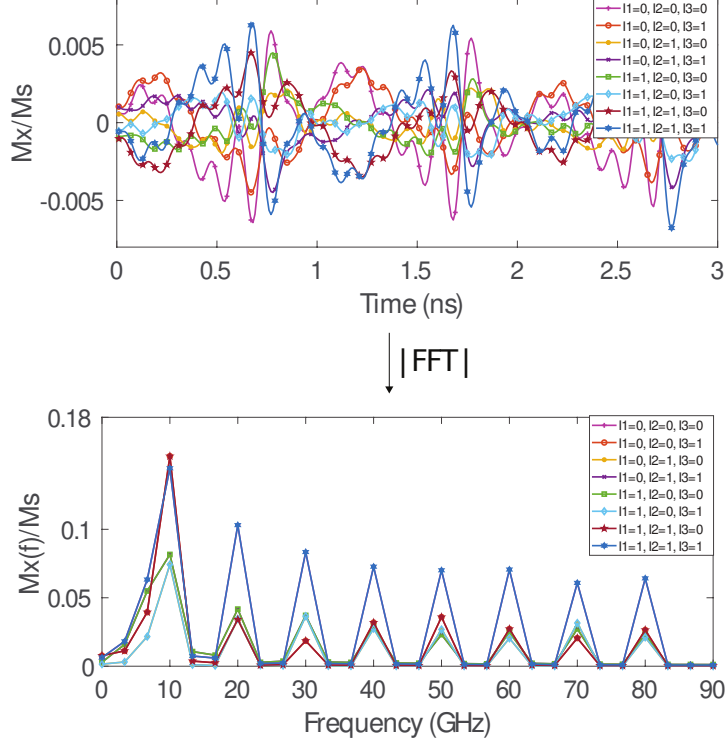


FIG. 11. Unoptimized 8-bit Majority Gate Time and Frequency Response.

at all frequencies is higher as the spin waves propagate on lower distances when compared with the non-optimized case. In addition, the detection threshold values are higher, i.e., $0.007 M_s$, $0.005 M_s$, $0.0045 M_s$, $0.0038 M_s$, $0.0034 M_s$, 0.0027 , $0.0025 M_s$, and $0.002 M_s$, therefore, less sensitive detectors are required for the XOR/XNOR gate implementation.

8-bit phase detection based 3-input Majority gate

The 8-bit 3-input unoptimized Majority gate OOMMF simulation results are presented in Figure 11. The same notations are in place and again, to simplify the Figure we only assume all 0s and all 1s input sets, thus only 8 input combinations are presented. The Figure clearly demonstrate proper gate functionality as 8 different frequencies components exist without distorting each-other in the Fast Fourier Transform (FFT) amplitude spectrum for all the possible input combinations $(\mathcal{I}_1 = \mathcal{I}_2 = \mathcal{I}_3 = 0)$, $(\mathcal{I}_1 = \mathcal{I}_2 = 0, \mathcal{I}_3 = 1)$, \dots , $(\mathcal{I}_1 = \mathcal{I}_2 = \mathcal{I}_3 = 1)$. Figure 12 indicates that the output SWs are not distorted and can be properly detected for each frequency. Let us concentrate on Figure 12a, which captures the 10 GHz 3-input Majority gate response and consider the output at time moment 0.75 ns,

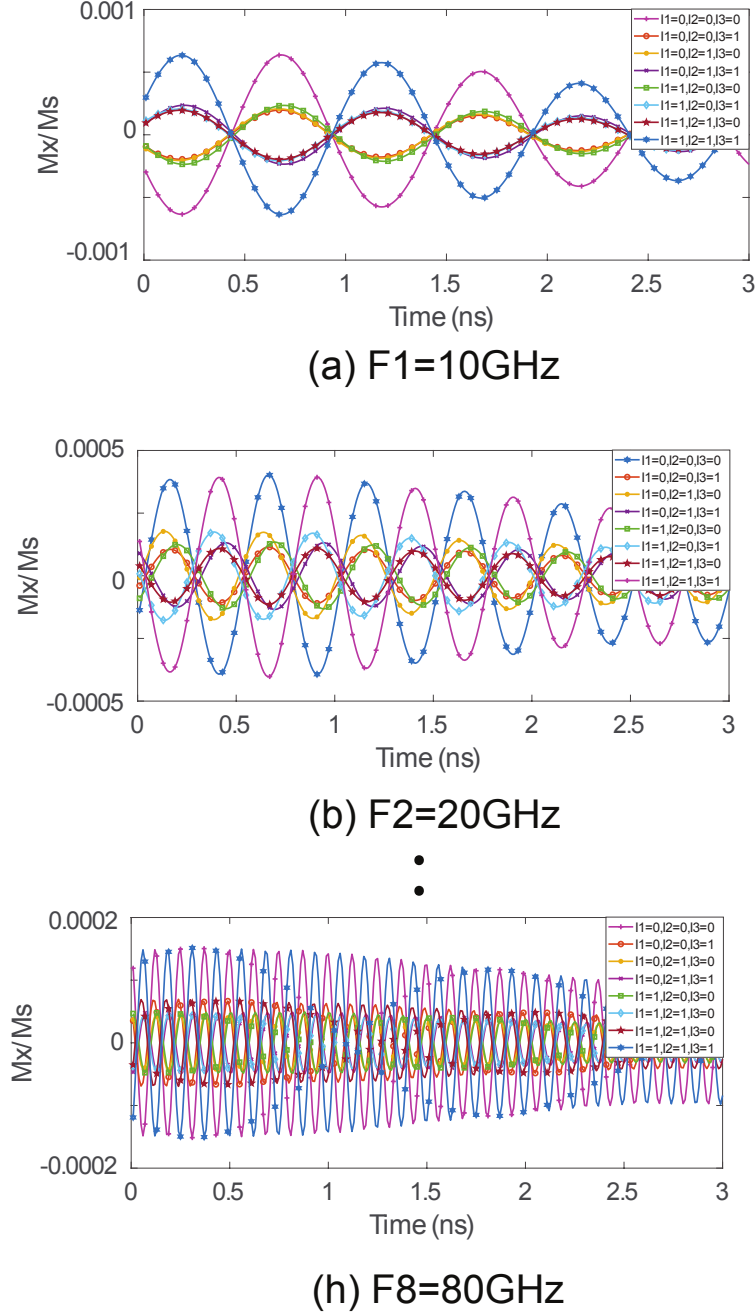


FIG. 12. Unoptimized 8-bit Majority Gate Outputs a) $f_1=10\text{ GHz}$, b) $f_2=20\text{ GHz}$, ..., h) $f_8=80\text{ GHz}$.

When the three inputs have the same phase of 0 ($I_1I_2I_3 = 000$) they constructively interfere in the waveguide resulting in a phase of 0 SW, which corresponds to a logic 0. Also, when at most one of the inputs is logic 1 ($I_1I_2I_3 = 001$, $I_1I_2I_3 = 010$, $I_1I_2I_3 = 100$), i.e., has phase of π , the SWs interfere constructively and destructively, and the results is still a logic 0. In

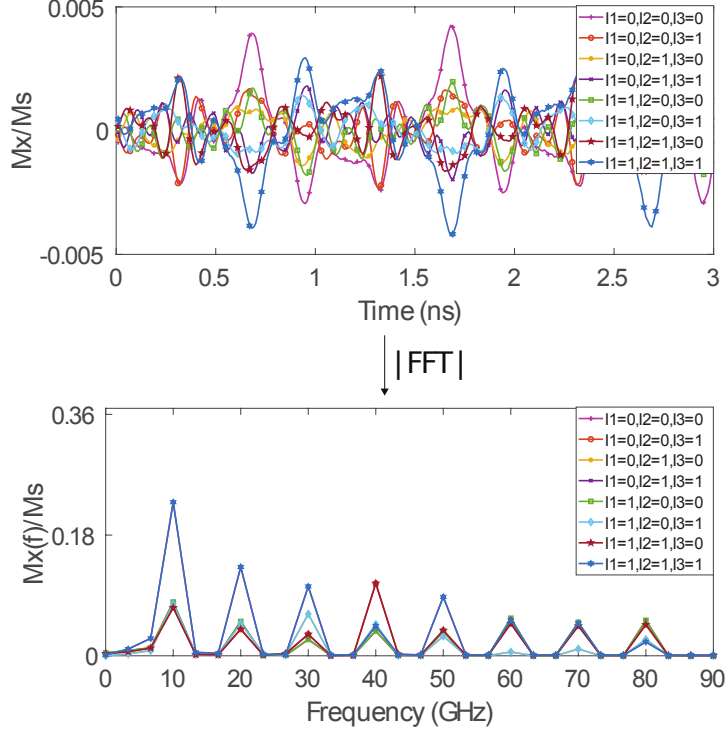


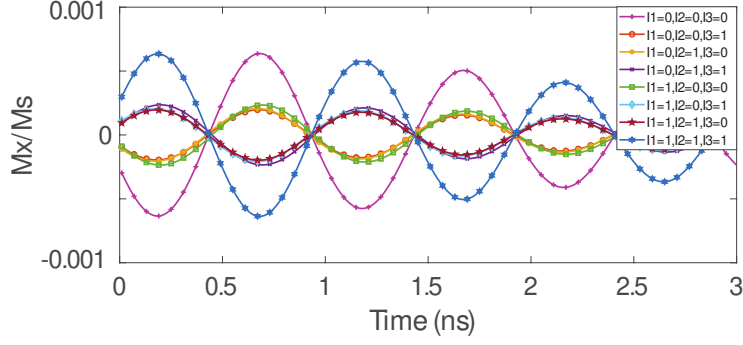
FIG. 13. Optimized 8-bit Majority Gate Time and Frequency Response.

contrast, if at most one of the inputs is logic 0 ($I_1I_2I_3 = 011$, $I_1I_2I_3 = 110$, $I_1I_2I_3 = 101$), then the output is logic 1 as a result of the interferences. Further, when the three inputs have the same phase of π ($I_1I_2I_3 = 111$), then spin waves interfere constructively in the waveguide, which results in a phase of π , which corresponds to a logic 1. The same line of reasoning can be applied for all the other 7 cases as it is clearly indicated by Figure 12.

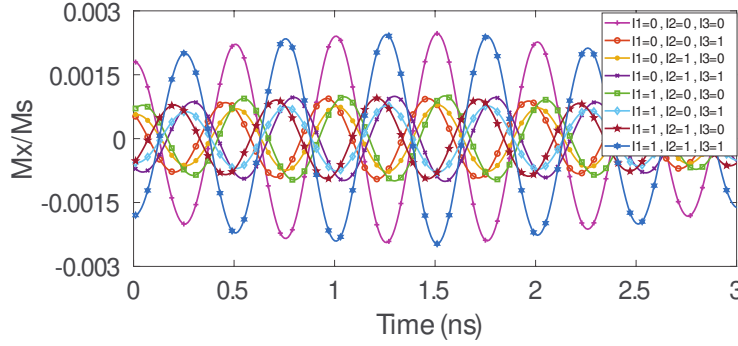
The optimized 8-input 3-input Majority gate OOMMF simulation results are presented in Figure 13 and 14. As it can be observed from Figure 14, the gate functions correctly while the SW amplitudes are higher as due to the optimization SWs propagate over shorter distances, which enables the utilization of less sensitive detectors.

B. Performance Evaluation

To get inside on the practical potential of our proposal, we evaluate and compare the 8-bit gates with functionally equivalent state-of-the-art SW implementation obtained by the instantiation of 8 normal (scalar) Majority/XOR gates, in terms of area, delay, and power consumption. In our evaluations we make the following assumptions: (i) source/detector

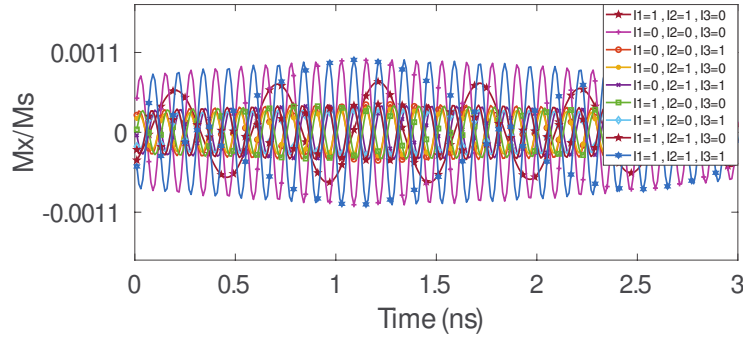


(a) $F1=10\text{GHz}$



(b) $F2=20\text{GHz}$

⋮



(h) $F8=80\text{GHz}$

FIG. 14. Optimized 8-bit Majority Gate Outputs a) $f_1=10\text{ GHz}$, b) $f_2=20\text{ GHz}$, . . . , h) $f_8=80\text{ GHz}$.

dimensions are $10\text{ nm} \times 50\text{ nm}$ as suggested in⁴⁶, (ii) SW propagation through the waveguide doesn't consume noticeable energy, and (iii) transducer delay is 0.42 ns ⁴⁹.

Under this assumptions we first evaluate the optimization algorithm impact on the 8-bit gates area. Our calculations indicate that the unoptimized XOR and Majority gates have an area of $0.025\ 25\ \mu\text{m}^2$ and $0.047\ 25\ \mu\text{m}^2$, respectively, which become $0.017\ 55\ \mu\text{m}^2$ and

0.0279 μm^2 , respectively, after the optimization. This clearly proves the algorithm efficiency as it diminishes the area by 30% and 41%, respectively.

As the standard functionally equivalent implementations require 8 2-input XOR and 8 3-input Majority gates it occupies 0.0784 μm^2 and 0.116 μm^2 real estate, respectively, our proposal enables a 4.47x and 4.16x area reduction, respectively.

Generally speaking, to calculate an SW gate delay one needs to sum-up the time associated to SW generation, propagation, and detection. The due to SW propagation through the waveguide delay depends on the travelled distance from generation to detection and it can be computed by dividing the distance by the SW group velocity, which is 3500 m/s for CoFeB⁴³. Given that the longest propagation path for the 8-bit 2-input XOR and 3-input Majority gates is 351 nm and 558 nm, respectively, the propagation delay is 100 ps and 159 ps, respectively, which by adding the transducers delay sums up to 940 ps and 999 ps, respectively. For the scalar 2-input XOR and 3-input Majority gates the longest path is 196 nm and 290 nm, respectively, which translates into a transmission delay of 56 ps and 83 ps, respectively, and 896 ps and 923 ps overall gate delay, respectively. Thus, the 8-bit 2-input XOR and 3-input Majority gates are slower than their scalar counterparts with 5% and 7%, respectively.

As both parallel and scalar gate implementations make use of the same number of transducers and the through the waveguide propagation consumes insignificant power, the two implementations are equivalent in terms of power consumption.

C. Fan-in and Geometrical Scalability

The proposed structure is generic and the number of bits per frequency, i.e., the gate fan-in, shouldn't affect its functionality. However, as the number of inputs increases, the damping effect might play a more significant role in diminishing SW amplitudes. Thus, if a large number of inputs is targeted, it might be needed to excite the same frequency SW inputs in Figure 6 at different energy levels $E_n < E_{n-1} < \dots < E_1$, where E_i is the energy that the i^{th} SW is excited at. We note however that: (i) usual fan-in values are rather small (2 and 3 in the gates we designed), (ii) energy level differentiation is only required for large fan-in values in case the logic gate doesn't function correctly, and (iii) within certain limits the SW energy levels can be adjusted by properly biasing the source transducers.

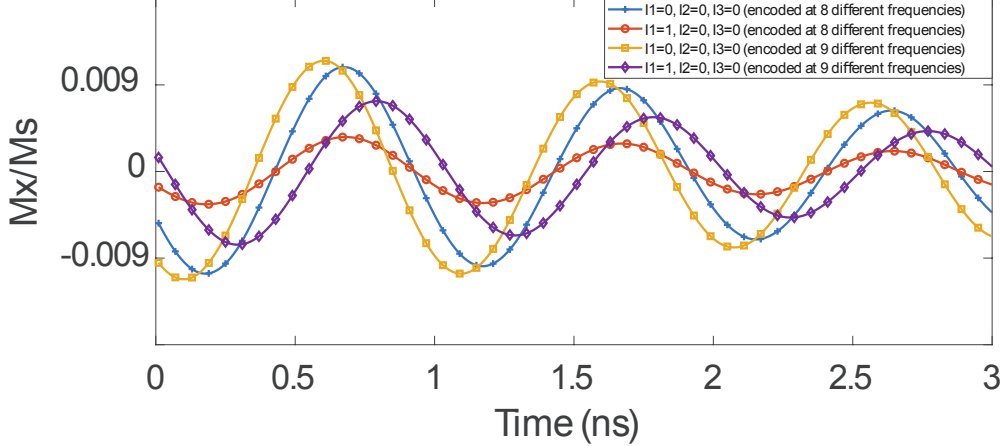


FIG. 15. MAJ Gate Outputs at $f_1=10\text{GHz}$.

To get inside on the effect of the waveguide width on gate functionality we scaled it from 50 nm up to 500 nm. It was noticed that scaling doesn't affect the gates functionality and it doesn't generate any crosstalk effects. We note that, as waveguide width increases, the ferromagnetic resonance frequency decreases and thus lower SW frequencies can be utilized. Although this is advantageous from signal loss perspective such structures require stronger static magnetic fields, which results in area and energy consumption overheads.

D. Practically Achievable Parallelism

To get some inside on the data parallelism practical upper-bound we examined the consequences of increasing the number of bits per set, i.e., utilized frequencies. To this end we OOMMF simulate 8-bit and 9-bit 3-input Majority gate instances and display in Figure 15 the 10 GHz frequency output component for the input combinations $\mathcal{I}_1\mathcal{I}_2\mathcal{I}_3 = 000$ and $\mathcal{I}_1\mathcal{I}_2\mathcal{I}_3 = 100$.

One can observe in the Figure that at time=0.5 ns the 8-bit Majority gate output has the same phase for the considered input combination, which reflects the correct functionality of the Majority gate as in both cases 0 is the majority. However, the 9-bit Majority gate output at time=0.5 ns has different phase, 0 for $\mathcal{I}_1\mathcal{I}_2\mathcal{I}_3 = 000$, and approximately $\pi/4$ for $\mathcal{I}_1\mathcal{I}_2\mathcal{I}_3 = 100$, which indicate that the gate starts to malfunction. Based on this we can conclude that, for the proposed topology and utilized material, 8 is the maximum number of frequencies one can use to construct robust parallel SW gates.

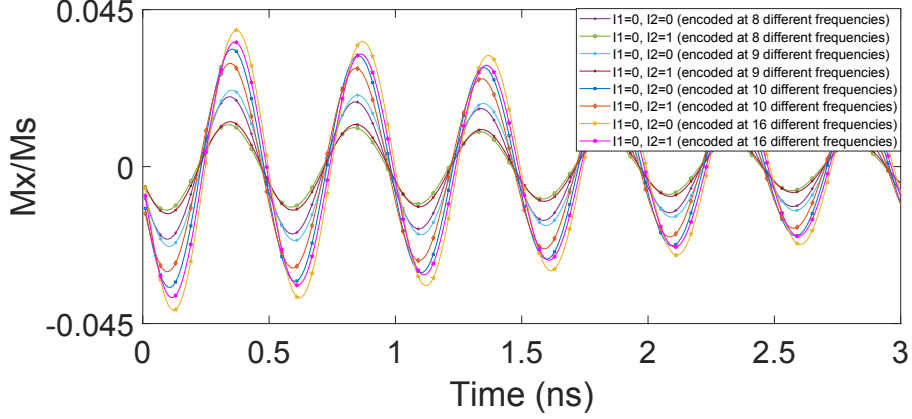


FIG. 16. XOR Gate Outputs at $f_2=20\text{GHz}$.

However, one can go beyond this limit if threshold detection based it utilized. To examine the effect of embedding more than 8 frequencies we evaluate by means of OOMMF simulations 2-input XOR gates with 8, 9, 10, and 16 frequencies. For illustration purpose we display in Figure 16 the 20 GHz frequency output component for the input combinations $\mathcal{I}_1\mathcal{I}_2 = 00$ and $\mathcal{I}_1\mathcal{I}_2 = 01$, which should give a 0 and 1 output value, respectively, for all the considered input widths. The Figure clearly indicates that while the spin wave magnetization difference between the two input combinations decreases as the number of frequency increases, which makes output detection more challenging, two different levels can still be distinguished and a threshold defined, as such if the spin wave magnetization is greater than that threshold, the output is 0, and 1 otherwise. To clarify this let us inspect the output value at time moment 0.4ns for the 8, 9, 10, and 16-bit XOR gates. For the input combination $\mathcal{I}_1\mathcal{I}_2 = 00$ the output SW has a higher amplitude than the one corresponding to $\mathcal{I}_1\mathcal{I}_2 = 01$, which means that a threshold can be set and based on threshold detection, X(N)OR can be detected. This suggests that for threshold detection based gates are more robust and can operate with up to 16-bit inputs. Note that more than 16-bit inputs might be realizable but it is part of planned future work.

Figure 17 presents OOMMF simulation results for the 16-bit based 2-input XOR gate. As it can be observed from the FFT magnitude spectrum in Figure 17, the information is encoded in SWs with 16 different frequencies, 10, 20, \dots , 160 GHz and the output for all the possible input combinations $(\mathcal{I}_1 = \mathcal{I}_2 = 0), \dots, (\mathcal{I}_1 = \mathcal{I}_2 = 1)$ can be detected at each frequency. To further examine the results, we filter each frequency component for different

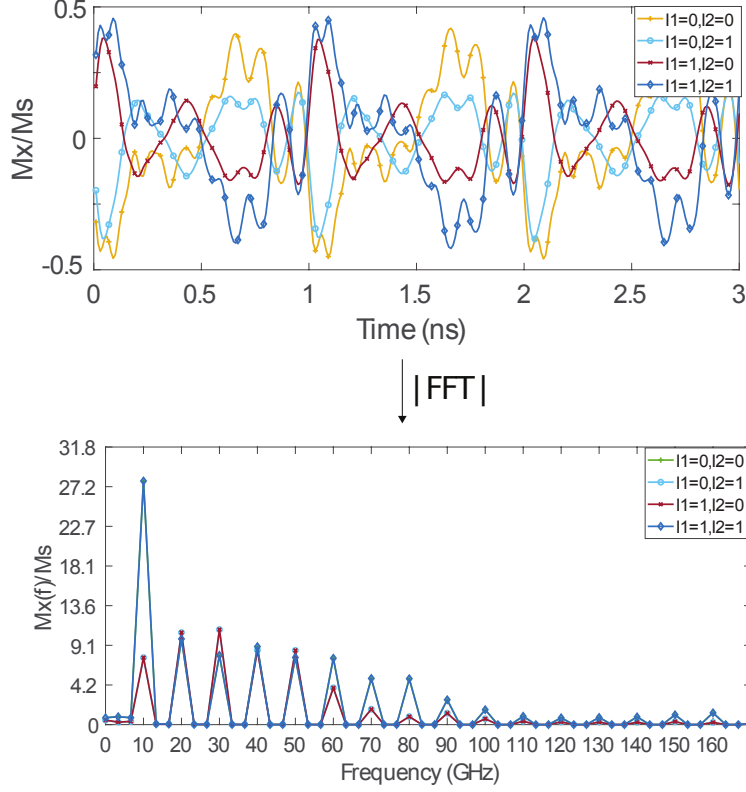


FIG. 17. Optimized 16-bit Majority Gate Response in Time and Frequency.

input combinations separately in Figure 18 and one can observe that the output SWs are not distorted and can be properly detected at each frequency, which means that the 16-bit XOR/XNOR gate operates correctly. Let us consider the 20 GHz output time moment 0.75 ns and a detection threshold value of $0.04 M_s$. For $\mathcal{I}_1 = \mathcal{I}_2 = 0$, or $\mathcal{I}_1 = \mathcal{I}_2 = 1$ the absolute SW magnetization value is greater than $0.04 M_s$ due to the constructive interference, which means 0 logic output as it should. For $\mathcal{I}_1 = 0\mathcal{I}_2 = 1$, or $\mathcal{I}_1 = 1\mathcal{I}_2 = 0$ the absolute SW magnetization value is lower than $0.04 M_s$, which means a 1 logic output as it should.

An XNOR can be realized by flipping the condition such that a SW magnetization lower (greater) than $0.04 M_s$ is read as a logic 0 (1). The same line of reasoning can be utilized to determine all threshold values as, $0.045 M_s$, $0.04 M_s$, $0.038 M_s$, $0.033 M_s$, $0.032 M_s$, $0.03 M_s$, $0.028 M_s$, $0.025 M_s$, $0.02 M_s$, $0.015 M_s$, $0.01 M_s$, $0.007 M_s$, $0.0068 M_s$, $0.005 M_s$, $0.0045 M_s$, $0.004 M_s$, $0.0035 M_s$, and $0.002 M_s$, for value increasingly ordered frequencies.

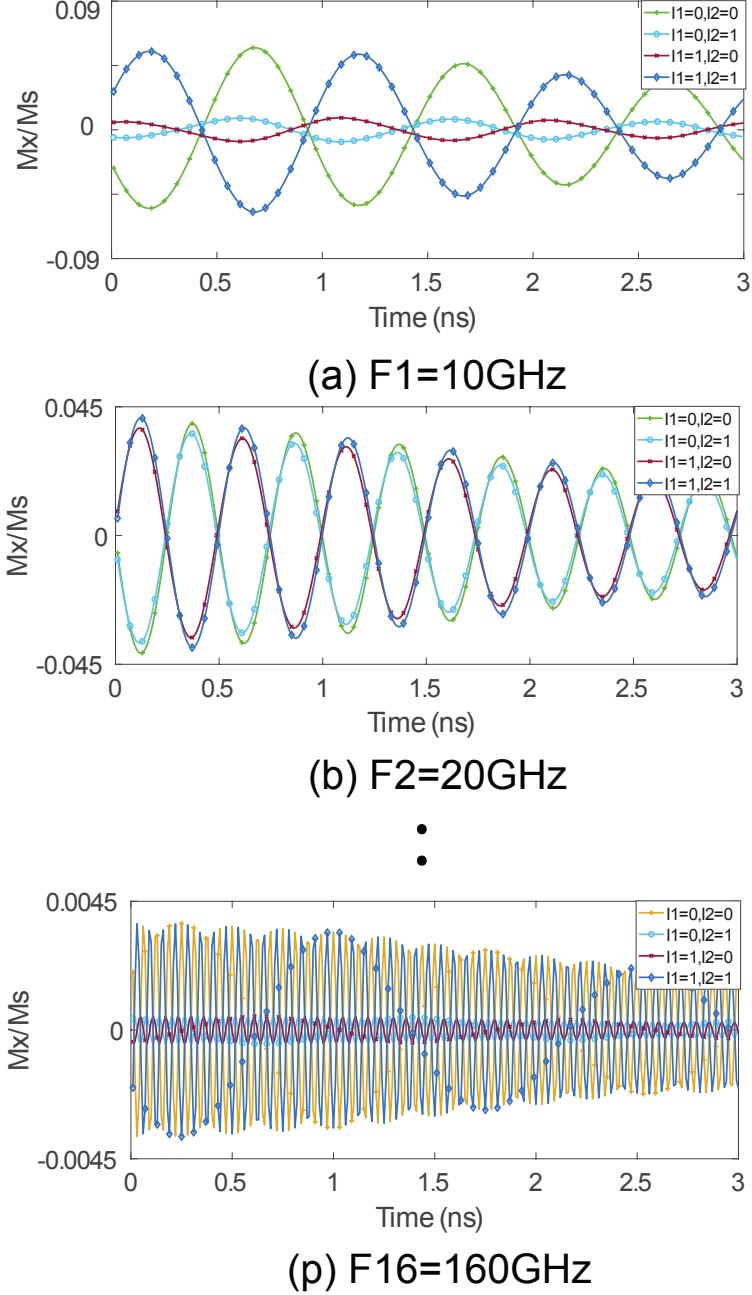


FIG. 18. Optimized XOR Gate Outputs: a) $f_1=10\text{ GHz}$, b) $f_2=20\text{ GHz}$, \dots , p) $f_{16}=160\text{ GHz}$.

E. Variability and Thermal Noise Effects

In this paper, our main purpose is to propose and validate an intrinsic data parallel spin wave technology under ideal conditions as a proof of concept, while disregarding factors, e.g., edge roughness, waveguide dimension variations, spin wave strength variation, and thermal noise, which might negatively affect the performance of the proposed concept. However,

in^{50,51}, the effects of waveguide trapezoidal cross section and edge roughness were investigated and demonstrated that they have a rather limited impact in gate behavior, which preserve functionality under their presence. Moreover, an investigation of a SW gate behaviour at different temperatures was presented in⁵⁰. At different temperatures, it was noticed that the gate functions correctly and that the temperature variation effect is rather limited. In addition to that, as our proposed structure is in-line waveguide width variations do not affect gate functionality, thus we expected it to be rather robust to dimension variations. Despite that fact that we expect that variability and thermal noise do not fundamentally affect the proposed gate behaviour, a thorough investigation of such effects is part of the planned future work.

VI. CONCLUSIONS

A novel n -bit data parallel spin wave logic gate was proposed in this paper. In order to explain the proposed concept, we implemented and validated by means of OOMMF, 8-bit 2-input XOR and 3-input Majority gates. Further, we proposed an optimization algorithm to minimize the area overhead of the proposed multi-frequency gates and demonstrate that the algorithm diminishes the area by 30% and 41% for XOR and MAJ gates implementations, respectively. Moreover, to assess the potential of our proposal, we evaluated and compared the proposed multifrequency gates with functionally equivalent scalar SW gate based implementations in terms of area, delay, and power consumption. The results indicated that the byte-based XOR and Majority gates require 4.47x and 4.16x area less than the conventional (scalar) implementations, respectively, at the expense of 5% to 7% delay overhead and without inducing any power consumption overhead. Finally, we demonstrated that, for current gate topology and materials, the maximum number of frequencies (gate parallelism) is 8 and 16 for phase and threshold based output detection, respectively.

ACKNOWLEDGEMENT

This work has received funding from the European Union's Horizon 2020 research and innovation program within the FET-OPEN project CHIRON under grant agreement No. 801055. It has also been partially supported by imec's industrial affiliate program on

beyond-CMOS logic. F.V. acknowledges financial support from Flanders Research Foundation (FWO) through grant No. 1S05719N.

REFERENCES

- ¹N. D. Shah, E. W. Steyerberg, and D. M. Kent, *JAMA* (2018).
- ²R. L. Villars, C. W. Olofson, and M. Eastwood, *IDC* (2011).
- ³S. Agarwal, G. Burr, A. Chen, S. Das, E. Debenedictis, M. P. Frank, P. Franzon, S. Holmes, M. Marinella, and T. Rakshit, “International roadmap of devices and systems 2017 edition: Beyond cmos chapter.” Tech. Rep. (Sandia National Lab.(SNL-NM), Albuquerque, NM (United States), 2018).
- ⁴D. Mamaluy and X. Gao, *Applied Physics Letters* **106**, 193503 (2015).
- ⁵B. Hoefflinger, *Chips 2020: a guide to the future of nanoelectronics* (Springer Science & Business Media, 2012).
- ⁶N. Z. Haron and S. Hamdioui, in *Design and Test Workshop, 2008. IDT 2008. 3rd International* (IEEE, 2008) pp. 98–103.
- ⁷Y. Jiang, N. C. Laurenciu, H. Wang, and S. D. Cotofana, *IEEE Transactions on Nanotechnology* **18**, 287 (2019).
- ⁸Y. Jiang, N. Cucu Laurenciu, and S. D. Cotofana, *IEEE Transactions on Circuits and Systems I: Regular Papers* **66**, 1948 (2019).
- ⁹S. Choudhary and S. Khandate, *IEEE Transactions on Nanotechnology* **18**, 670 (2019).
- ¹⁰Y. Jiang, N. C. Laurenciu, H. Wang, and S. D. Cotofana, *IEEE Transactions on Nanotechnology* **18**, 287 (2019).
- ¹¹S. Bansal, A. Das, P. Jain, K. Prakash, K. Sharma, N. Kumar, N. Sardana, N. Gupta, S. Kumar, and A. K. Singh, *IEEE Transactions on Nanotechnology* **18**, 781 (2019).
- ¹²H. Nili, A. F. Vincent, M. Prezesio, M. R. Mahmoodi, I. Kataeva, and D. B. Strukov, *IEEE Transactions on Nanotechnology* **19**, 344 (2020).
- ¹³S. N. Truong, K. Van Pham, and K. Min, *IEEE Transactions on Nanotechnology* **17**, 482 (2018).
- ¹⁴C. E. Graves, C. Li, X. Sheng, W. Ma, S. R. Chalamalasetti, D. Miller, J. S. Ignowski, B. Buchanan, L. Zheng, S. Lam, X. Li, L. Kiyama, M. Foltin, M. P. Hardy, and J. P. Strachan, *IEEE Transactions on Nanotechnology* **18**, 963 (2019).

- ¹⁵N. Zheng and P. Mazumder, IEEE Transactions on Nanotechnology **17**, 520 (2018).
- ¹⁶M. R. Mahmoodi, A. F. Vincent, H. Nili, and D. B. Strukov, IEEE Transactions on Nanotechnology **19**, 429 (2020).
- ¹⁷K. P. Gnawali, S. N. Mozaffari, and S. Tragoudas, IEEE Transactions on Nanotechnology **17**, 1206 (2018).
- ¹⁸H. Zhang, W. Kang, B. Wu, P. Ouyang, E. Deng, Y. Zhang, and W. Zhao, IEEE Transactions on Nanotechnology **18**, 473 (2019).
- ¹⁹D. Zhang, Y. Hou, L. Zeng, and W. Zhao, IEEE Transactions on Nanotechnology **18**, 518 (2019).
- ²⁰S. K. Thirumala, Y. Hung, S. Jain, A. Raha, N. Thakuria, V. Raghunathan, A. Raghunathan, Z. Chen, and S. K. Gupta, IEEE Transactions on Nanotechnology , 1 (2020).
- ²¹A. Roohi and R. F. DeMara, IEEE Transactions on Nanotechnology **18**, 885 (2019).
- ²²D. E. Nikonov and I. A. Young, Proceedings of the IEEE **101**, 2498 (2013).
- ²³M. P. Kostylev, A. A. Serga, T. Schneider, B. Leven, and B. Hillebrands, Applied Physics Letters **87**, 153501 (2005), <https://doi.org/10.1063/1.2089147>.
- ²⁴T. Schneider, A. A. Serga, B. Leven, B. Hillebrands, R. L. Stamps, and M. P. Kostylev, Applied Physics Letters **92**, 022505 (2008), <https://doi.org/10.1063/1.2834714>.
- ²⁵K.-S. Lee and S.-K. Kim, Journal of Applied Physics **104**, 053909 (2008), <https://doi.org/10.1063/1.2975235>.
- ²⁶I. A. Ustinova, A. A. Nikitin, A. B. Ustinov, B. A. Kalinikos, and E. Lähderanta, in *2017 11th International Workshop on the Electromagnetic Compatibility of Integrated Circuits (EMCCompo)* (2017) pp. 104–107.
- ²⁷A. Khitun and K. L. Wang, Superlattices and Microstructures **38**, 184 (2005).
- ²⁸Y. Wu, M. Bao, A. Khitun, J.-Y. Kim, A. Hong, and K. L. Wang, Journal of Nanoelectronics and Optoelectronics **4**, 394 (2009).
- ²⁹A. Khitun, D. E. Nikonov, M. Bao, K. Galatsis, and K. L. Wang, Nanotechnology **18**, 465202 (2007).
- ³⁰A. Khitun, M. Bao, Y. Wu, J. Kim, A. Hong, A. Jacob, K. Galatsis, and K. L. Wang, in *Fifth International Conference on Information Technology: New Generations (itng 2008)* (2008) pp. 1107–1110.
- ³¹B. Rana and Y. Otani, Phys. Rev. Applied **9**, 014033 (2018).

- ³²A. V. Chumak, A. A. Serga, and B. Hillebrands, *Journal of Physics D: Applied Physics* **50**, 244001 (2017).
- ³³A. Khitun and K. L. Wang, *Journal of Applied Physics* **110**, 034306 (2011), <https://doi.org/10.1063/1.3609062>.
- ³⁴S. Klingler, P. Pirro, T. Brächer, B. Leven, B. Hillebrands, and A. V. Chumak, *Applied Physics Letters* **105**, 152410 (2014), <https://doi.org/10.1063/1.4898042>.
- ³⁵S. Klingler, P. Pirro, T. Brächer, B. Leven, B. Hillebrands, and A. V. Chumak, *Applied Physics Letters* **106**, 212406 (2015).
- ³⁶O. Zografos, S. Dutta, M. Manfrini, A. Vaysset, B. Sorée, A. Naeemi, P. Raghavan, R. Lauwereins, and I. P. Radu, *AIP Advances* **7**, 056020 (2017), <https://doi.org/10.1063/1.4975693>.
- ³⁷K. Nanayakkara, A. Anferov, A. P. Jacob, S. J. Allen, and A. Kozhanov, *IEEE Transactions on Magnetics* **50**, 1 (2014).
- ³⁸T. Fischer, M. Kewenig, D. A. Bozhko, A. A. Serga, I. I. Syvorotka, F. Ciubotaru, C. Adelman, B. Hillebrands, and A. V. Chumak, *Applied Physics Letters* **110**, 152401 (2017), <https://doi.org/10.1063/1.4979840>.
- ³⁹P. Shabadi, A. Khitun, P. Narayanan, M. Bao, I. Koren, K. L. Wang, and C. A. Moritz, in *2010 IEEE/ACM International Symposium on Nanoscale Architectures* (2010) pp. 11–16.
- ⁴⁰T. Fischer, M. Kewenig, D. A. Bozhko, A. A. Serga, I. I. Syvorotka, F. Ciubotaru, C. Adelman, B. Hillebrands, and A. V. Chumak, *Applied Physics Letters* **110**, 152401 (2017), <https://doi.org/10.1063/1.4979840>.
- ⁴¹F. Ciubotaru, G. Talmelli, T. Devolder, O. Zografos, M. Heyns, C. Adelman, and I. P. Radu, in *2018 IEEE International Electron Devices Meeting (IEDM)* (2018) pp. 36.1.1–36.1.4.
- ⁴²A. Khitun, *Journal of Applied Physics* **111**, 054307 (2012), <https://doi.org/10.1063/1.3689011>.
- ⁴³A. V. Chumak, A. A. Serga, and B. Hillebrands, *Journal of Physics D: Applied Physics* **50**, 244001 (2017).
- ⁴⁴L. Landau and E. Lifshitz., *Phys. Z. Sowjetunion* , 101 (1935).
- ⁴⁵T. L. Gilbert, *IEEE Transactions on Magnetics* **40**, 3443 (2004).
- ⁴⁶A. Mahmoud, F. Vanderveken, F. Ciubotaru, C. Adelman, S. Cotofana, and S. Hamdioui, in *2020 Design, Automation Test in Europe Conference Exhibition (DATE)* (2020) pp.

642–645.

- ⁴⁷M. J. Donahue and D. G. Porter, Interagency Report NISTIR 6376 (1999).
- ⁴⁸T. Devolder, J.-V. Kim, F. Garcia-Sanchez, J. Swerts, W. Kim, S. Couet, G. Kar, and A. Furnemont, *Phys. Rev. B* **93**, 024420 (2016).
- ⁴⁹O. Zografos, B. Sorée, A. Vaysset, S. Cosemans, L. Amarù, P. Gaillardon, G. D. Micheli, R. Lauwereins, S. Sayan, P. Raghavan, I. P. Radu, and A. Thean, in *2015 IEEE 15th International Conference on Nanotechnology (IEEE-NANO)* (2015) pp. 686–689.
- ⁵⁰Q. Wang, P. Pirro, R. Verba, A. Slavin, B. Hillebrands, and A. V. Chumak, *Science Advances* **4** (2018), 10.1126/sciadv.1701517, <https://advances.sciencemag.org/content/4/1/e1701517.full.pdf>.
- ⁵¹Q. Wang, B. Heinz, R. Verba, M. Kewenig, P. Pirro, M. Schneider, T. Meyer, B. Lägél, C. Dubs, T. Brächer, and A. V. Chumak, *Phys. Rev. Lett.* **122**, 247202 (2019).